Properties of Steady Geostrophic Turbulence with Isopycnal Outcropping

G. ROULLET

Laboratoire de Physique des Oceans, Brest, France, and IGPP, University of California, Los Angeles, Los Angeles, California

J. C. MCWILLIAMS

IGPP, University of California, Los Angeles, Los Angeles, California

X. CAPET

Laboratoire de Physique des Oceans, Brest, France

M. J. MOLEMAKER

IGPP, University of California, Los Angeles, Los Angeles, California

ABSTRACT

High-resolution simulations of β-channel, zonal-jet, baroclinic turbulence with a three-dimensional quasigeostrophic (QG) model including surface potential vorticity (PV) are analyzed with emphasis on the competing role of interior and surface PV (associated with isopycnal outcropping). Two distinct regimes are considered: a Phillips case, where the PV gradient changes sign twice in the interior, and a Charney case, where the PV gradient changes sign in the interior and at the surface. The Phillips case is typical of the simplified turbulence test beds that have been widely used to investigate the effect of ocean eddies on ocean tracer distribution and fluxes. The Charney case shares many similarities with recent high-resolution primitive equation simulations. The main difference between the two regimes is indeed an energization of submesoscale turbulence near the surface. The energy cycle is analyzed in the (k, z) plane, where k is the horizontal wavenumber. In the two regimes, the large-scale buoyancy forcing is the primary source of mechanical energy. It sustains an energy cycle in which baroclinic instability converts more available potential energy (APE) to kinetic energy (KE) than the APE directly injected by the forcing. This is due to a conversion of KE to APE at the scale of arrest. All the KE is dissipated at the bottom at large scales, in the limit of infinite resolution and despite the submesoscales energizing in the Charney case. The eddy PV flux is largest at the scale of arrest in both cases. The eddy diffusivity is very smooth but highly nonuniform. The eddy-induced circulation acts to flatten the mean isopycnals in both cases.

---

1. Introduction

Baroclinic instability (BCI) is the fundamental process responsible for the maintenance of the mesoscale eddy-rich, quasi-balanced turbulence in the ocean, outside of the equatorial band (Gill et al. 1974; Stammer 1997). From a linear perspective, the Charney–Stern–Pedlosky criterion states that for BCI to occur the meridional potential vorticity (PV) gradient Q_y of a zonal jet has to change sign in the vertical. In the fully developed regime,

this argument is less clear because PV is so fine grained that attempts to access Q_y from real data yield noisy patterns, even with smooth climatological data (Marshall et al. 1993; Smith 2007). However, smoother new estimates allow Tulloch et al. (2011) to sketch a global map of zonally averaged Q_y as a function of latitude. Interestingly, in the sketch, there seems to be a pool of $Q_y < 0$, opposite to the β planetary PV gradient at all latitudes, except in the equatorial band, and with a vertical position depending on the latitude. This supports the linear argument that there should be regions of $Q_y < 0$ for the BCI to be sustained. Two qualitatively distinct cases can be considered: a high-latitude case where the pool of $Q_y < 0$ is in the interior and a midlatitude case where the pool

Corresponding author address: G. Roullet, Laboratoire de Physique des Oceans, UMR6523, 6 Ave Le Gorgeu, 29200 Brest, France.
E-mail: roullet@univ-brest.fr

hits the surface (Smith 2007; Tulloch et al. 2011). Incidentally, there always seems to be two changes of sign in the vertical rather than one. The former case corresponds to a purely interior BCI, which is somehow similar to the Phillips problem (Phillips 1954), though Phillips only considered one change of sign in the vertical. The latter case involves the so-called surface PV (Bretherton 1966) that encodes the isopycnal outcropping. It corresponds to a mixed surface–interior BCI and shares some similarity with the Charney problem (Charney 1947). Most of our understanding of geostrophic turbulence comes from the Phillips-like regime in which the surface PV is simply ignored. The Charney-like regime has been studied in recent primitive equation (PE) experiments (Klein et al. 2008; Zurita-Gotor and Vallis 2009) as well in a truncated quasigeostrophic (QG) model (Tulloch and Smith 2009). It seems to be much more energetic than the Phillips case with surface PV playing a central role in many aspects of the turbulence. The central goal of this paper is to rationalize the differences between these two regimes: surface–interior versus interior–interior BCI. Following Smith (2007), we will call them the Charney case and the Phillips case, respectively. The paper is in spirit the continuation of two-layer or few-layer QG experiments (Salmon 1980; McWilliams and Chow 1981; Held and Larichev 1996; Smith and Vallis 2002), with an attempt to bridge the gap with recent PE simulations (Klein et al. 2008). It reviews the properties of quasigeostrophic turbulence and compares these two regimes using high-resolution experiments with an emphasis on the vertical aspects.

In section 2, we describe the design of two numerical idealized experiments that differ by the presence or not of surface PV and that retain the main features of the Southern Ocean (SO): a baroclinically unstable eastward jet and a realistic mean stratification. However, two major ingredients are completely absent: bottom topography, which modifies the bottom drag and strongly controls the barotropic dynamics (Tréguier and McWilliams 1990; Hogg and Blundell 2006), and equatorward connection of the jet with the meridional overturning circulation, which importantly influences the residual circulation (RC; Marshall and Radko 2003; Abernathey et al. 2011). The forcing procedure is also disputable; it restores to a prescribed reference state that imposes an artificial diabatic forcing in the interior. There is also no mixed layer: QG is unable to handle vanishing vertical stratification. These deficiencies prevent our understanding the SO as a whole. The purpose of this paper is to focus on one particular aspect of geostrophic turbulence: the role of the isopycnal outcropping. We took great care in the design of the model and the experiments in the following ways: we used a very accurate advection scheme for PV; convergence tests with increase of resolution; uniformly high resolution in both

horizontal and stretched vertical coordinates; an original averaging procedure of the forcing that enforces a large-scale steady forcing; and a zonally periodic channel geometry (as opposed to biperiodic) that allows the buoyancy to have a mean gradient in the meridional direction.

In section 3, we show how the surface PV in the Charney case qualitatively changes the properties of the BCI by escaping the high-wavenumber cutoff for unstable modes. In section 4, we describe the properties of PV and vorticity. In section 5, we put forward the main result of this paper: based on an analysis of the energy budget in the semispectral plane (k, z), we show there is an energy loop that differs from Salmon's (1980) diagram. BCI converts more available potential energy (APE; by roughly a factor of 3) than the forcing puts in because the barotropic eddies at the scale of arrest convert kinetic energy (KE) back to APE. The conversion occurs over a range of scales rather than only at the scale of the most unstable mode. In section 6, we present the eddy diffusivity and the eddy-induced (i.e., bolus) and residual circulations. The diffusivity is smooth but not uniform; it is intensified where $Q_y < 0$ is extremal compatible with a steering level argument (Green 1970; Killworth 1997; Smith and Marshall 2009; Abernathey et al. 2010). We discuss the eddy-induced circulation (EIC) in relation to outcropping in both vertical and density coordinates (Held and Schneider 1999). Conclusions are given in section 7.

2. Experimental framework

a. The domain

The domain is a zonally reentrant channel on the β plane with a flat bottom. The dimensions are $L \times 2L \times H$, where $L = 768$ km is the zonal width and $H = 4$ km is the total depth. The Coriolis parameter $f = 10^{-4}$ s^{-1} (chosen positive) and $\beta = 1.56 \times 10^{-11}$ m^{-1} s^{-1} are typical of a midlatitude. Here, L is used to nondimensionalize all the following horizontal wavenumbers: the wavenumber $k_0 = 1$ is associated with the zonal width L. The smallest available wavenumber in the domain is $k_0/2$ for the meridional direction.

b. Model equations

The numerical model solves the QG equations written for PV,

$$\partial_t q + J(\psi, q + \beta y) = F_q + D_q + E(\nabla^2 \psi); \quad (1)$$

$$\partial_t b + J(\psi, b) = F_b + D_b, \quad \text{at} \quad z = -H, 0; \quad \text{and} \quad (2)$$

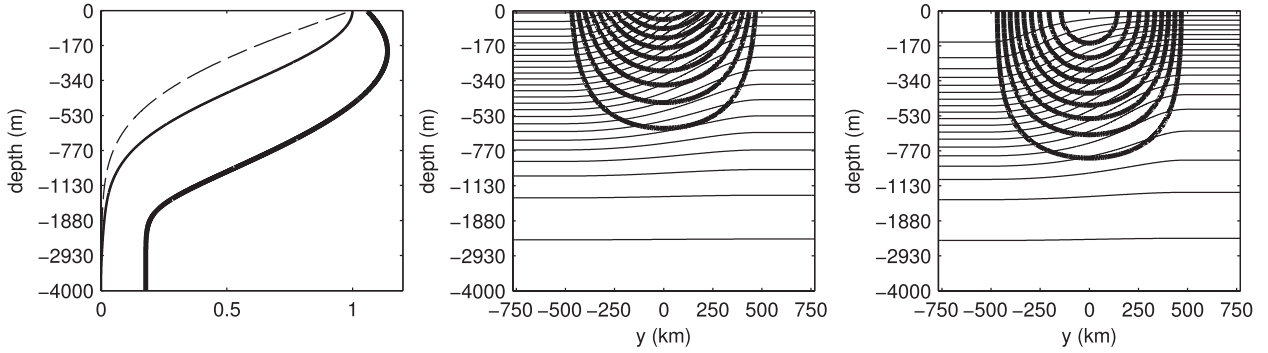$$\partial_t \Delta \Gamma = \int \int F_q + D_q + E[\nabla^2 \psi] \, dx \, dy, \quad (3)$$

FIG. 1. (left) Vertical profiles of $S(z)H/L_d$ (thick black) and $U(z)/U*\beta L_d^2$ for the Charney case (dashed) and the Phillips case (solid). (middle) Meridional section of the reference total buoyancy $b(y,z)H/(f^2L_d^2)$ [thin; contour interval (CI) = 0.05] and the associated jet zonal velocity $U(y,z)$ (thick; CI = 1 cm s^{-1}) for the Charney case. (right) Idem for the Phillips case. Vertical axis are uniform in stretched coordinates z'.

where ψ is the streamfunction; $q = \nabla^2\psi + \partial_z(S^{-2}\partial_z\psi)$ is the interior PV; $S(z) = N(z)/f$ is the stretching parameter; $N(z)$ is the mean stratification frequency; $b = f\partial_z\psi$ is the buoyancy; $\Delta\Gamma = \Gamma(L, z) - \Gamma(-L, z)$ is the difference of circulation $\Gamma(y, z) = \int \partial_y\psi\, dx$ between the two walls; $F_{b,q}$ ($D_{b,q}$) is the forcing (small-scale dissipation) on buoyancy and PV; $E(\phi) = -\lambda\delta(z + H)$; φ is the linear bottom drag with parameter λ; and $\delta(z)$ is the Dirac delta function. These equations are integrated forward in time. At each time step, ψ is computed by inverting the PV using the boundary conditions (b for the surface and the bottom and $\Delta\Gamma$ along the walls). Also note that, because of the properties of the F_q and D_q, Eq. (3) reduces to $\partial t\Delta\Gamma = \iint E(\nabla^2\psi)\, dx\, dy$ (see below).

The surface PV θ_s is related to the surface buoyancy b_s by $\theta_s = -S^{-2}(0)b_s$ (Bretherton 1966) and likewise for the bottom PV $\theta_b = +S^{-2}(-H)b_b$. The few-layer QG model consists of setting the surface and bottom PV to zero while keeping interior PV, whereas the surface QG model (Held et al. 1995) consists in the reverse. It is worth emphasizing that interior PV at the surface and the surface PV are two different quantities, although they live at the same place. They correspond to two independent degrees of freedom. The full QG model, as presented here, might be considered a coupled interior–surface QG model. Note too that the circulation along the walls can also be seen as lateral PV.

c. Mean stratification

The mean stratification $\overline{b}(z)$ is designed to be simple while retaining the principal features of the SO: a uniform weak stratification in the abyss, a strong pycnocline at intermediate depths, and a slight destratification near the surface (Fig. 1). There is no mixed layer because QG cannot handle vanishing N. The mean stratification is

$$\overline{b}(\tilde{z}) = \frac{(fL_d)^2}{H}b_0\langle 0.1\tilde{z} - b_1 + 0.5\{1 + \tanh[8(\tilde{z} - 0.95)]\}\rangle \qquad (4)$$

where $\tilde{z} = 1 + z/H$; b_0 and b_1 are two normalizing constants, and L_d is the deformation radius. The two constants are set so that $\overline{b}(0) = (fL_d)^2/H$ and $\overline{b}(-H) = 0$. The deformation radius is set to $L_d = 96$ km.[1] We denote k_d as the associated nondimensionalize wavenumber; it corresponds to $kd = 8$. Thus the domain width is much greater than the deformation radius, allowing the inverse cascade to develop. We will make intensive use of the stretched vertical coordinate $z'(z)$, defined with $dz' = S(z)$. The vertical discretization of the model is uniform in z', yielding a well-balanced PV operator. This coordinate compensates for the stratification; it magnifies vertical structures in the thermocline and shrinks them in the abyss. It will be used for the vertical axis in the figures.

d. Forcing

The forcing (on both PV and buoyancy) basically consists of restoring toward a zonally uniform reference state $b_{\rm ref}$, with a prescribed time scale τ. This reference state corresponds to a baroclinically unstable jet with a surface-intensified velocity $U(y, z; \alpha)$. Again, we designed an idealized jet profile, inspired from the SO; it allows us to vary the regime from a Charney to a Phillips by varying a single parameter α. To ensure smooth associated PV gradients, the velocity form is

---

[1] Note that the customary Rossby deformation radius, deduced from the Sturm–Liouville problem, is π times smaller than L_d.

$$G(\tilde{b}; \alpha) = 2(\alpha - 1)\tilde{b}^3 + (3 - 2\alpha)\tilde{b}^2 \qquad (5)$$

on the vertical, with $\tilde{b} = \tilde{b}H/(fL_d)^2$. To avoid side effects by interaction with the walls, the jet is confined to the center of the channel using a window function

$$F(\tilde{y}) = \begin{cases} \cos(\pi\tilde{y}), & |\tilde{y}| \geq 1/2 \\ 0, & |\tilde{y}| > 1/2 \end{cases}, \qquad (6)$$

where $\tilde{y} = y/L_{jet}$ and L_{jet} is the typical size of the jet, set to $L_{jet} = 600$ km. The jet velocity is then $U(y, z; \alpha) = U_0 F(\tilde{y})G(\tilde{b}; \alpha)$ with intensity $U_0 = U*\beta L_d^2$, controlled with the so-called nondimensional criticality parameter $U*$ (Held and Larichev 1996).

The parameter $\alpha \in [0, 1]$ is the main control parameter allowing a switch from a Phillips ($\alpha = 0$) to a Charney regime ($\alpha = 1$) (Fig. 1). It is worth emphasizing that, by looking only at $U(z)$, the two experiments seem very similar. They only differ by the vertical shear at surface. It will be manifest later that, despite this similarity, the regimes are dramatically different. For a given α, $U*$ controls the intensity of the jet and, via the thermal wind relation, the isopycnal slope and the buoyancy contrast between the northern and southern flanks of the jet $\Delta b(z)$ (Fig. 1). Bearing in mind that we want these experiments to be reproducible in a PE model, we require static stability for the total buoyancy vertical profiles, $\bar{b}(z) \pm \Delta b(z)/2$. This is clearly unnecessary for a QG model, but by doing so we constrain the setup to remain within reasonable bounds. In particular, for the chosen jet width, the

criticality cannot be too large. Even a moderate value of $U* = 2$ yields statically unstable profiles. We set $U* = 0.6$ for the two experiments, which corresponds to a jet velocity of $U \approx 8$ cm s^{-1}. From this velocity we define the β scale (i.e., Rhines scale), $L_\beta = \pi\sqrt{U_0/\beta} \approx 250$ km, and the nondimensional wavenumber $k_\beta = 3$. The π factor has been introduced to match an emerging scale of the experiments.

This restoring forcing, though frequently used in idealized studies (Klein et al. 2008; Zurita-Gotor and Vallis 2009), is highly unrealistic because there is no "spring" in the ocean interior. This somehow introduces an artificial feedback between the forcing and the flow. Having said that and recognizing that the structure of the forcing is of prime importance in a forced–dissipated problem, we have improved this classical forcing by adding three ingredients: (i) the forcing term is zonally averaged, (ii) this average is then convoluted in the meridional direction with a Hanning window $W(y; L_s)$ of width L_s, and (iii) the resulting convolution is time filtered using a recursive first-order filter with a memory parameter γ^{-1}.

Ingredients (ii) and (iii) are new and fix some of the drawbacks of a conventional restoring. Explicitly, we have

$$F_Q = -\tau^{-1}H(Q - Q_{ref}) \qquad (7)$$

with $Q = (b, q)$ and H the smoothing operator

$$H(Q) = C\int_0^L dx \int_{-L}^L dy \int_{-\infty}^t dt' e^{-\gamma(t-t')} W[(y - y')/L_s]Q(x', y'z, t'), \qquad (8)$$

where C is a normalization factor. Finally, to guarantee a zero PV forcing on average, we remove the symmetric part (in the meridional direction) of this term. Consequently, the forcing term on the circulation $\iint F_q \, dx \, dy$ vanishes. Note that the convolution does not involve the vertical direction. However, the resulting forcing turns out to be smooth in this direction too. The restoring time scale is $\tau = 50$ days; the memory parameter is set to $\gamma^{-1} = 50$ days; and the smoothing length scale is set to 600 km. Its associated wavenumber is $k_s \approx 1.3$. The forcing is still unrealistic and cannot be compared to the combination of wind stress and surface heat flux. It has, however, the nice property of being large scale ($k \leq k_s$) and almost steady in time. The forcing can be seen as a parameterization for large-scale unresolved processes that maintain the flow close to the reference state.

e. Small-scale dissipation

Equations (1)–(3) are integrated using a predictor corrector stepping scheme and a third-order upwind horizontal discretization for both PV and buoyancy advection (Shchepetkin and McWilliams 2005). We denote the discretized dissipative Jacobian as J_{diss}. As a result, explicit small-scale dissipation is not necessary and no tunable parameter sets its intensity. Although D_q cannot be written explicitly, we designed an original, general method to diagnose its effect on PV. It is based on a split between the reversible and nonreversible parts of the advection scheme,

$$D_q = \frac{1}{2\Delta t}[J_{diss}(\psi\Delta t, q) + J_{diss}(-\psi\Delta t, q)], \qquad (9)$$

where PV is advected forward in time over one time step Δt then backward to the initial time (appendix B). With

a perfect Jacobian, D_q would be zero. Being derived from the Jacobian term, D_q has no signature on the equation for the circulation $\iint D_q \, dx \, dy = 0$. Note also that D_q is not sign definite. In practice, it acts very similar to a biharmonic operator. This procedure is applied to the other variables (u, v, and b) (see next section).

f. The numerical experiments

The rest of the paper deals with the statistical steady turbulence for the two extreme regimes corresponding to a Phillips case ($\alpha = 0$) and a Charney case ($\alpha = 1$). (Appendix A has a complete list of all parameters and parameter values.) The spinup procedure described below was designed to obtain steady solutions at the highest possible resolution. It assumes (and this was verified) that finescale turbulence should not overly affect the larger-scale motions. The experiments are started from the reference state integrated over 850 days at 3-km resolution ($256 \times 256 \times 32$). Then two levels of resolution increase are performed: (i) from the restart at day 600, the model is integrated for 250 days at twice the resolution (1.5 km, $512 \times 1024 \times 64$); (ii) from the restart at day 650 at the 512 resolution, the resolution is doubled again (750 m, $1024 \times 2048 \times 128$) and integrated over 200 days. All the diagnostics are conducted over the final 200-day period. We have checked the steady state by looking at the time evolution of enstrophy, KE, and APE levels: they are oscillating in time, because of mesoscale variability, but no trend can be detected.

The grid is uniform horizontally and stretched vertically, $\Delta x = \Delta y = \Delta z'$. This implicitly sets the thickness Δz of the vertical levels: namely, $S(z)\Delta z = \Delta x$. This discretization ensures the three-dimensional (3D) isotropy and the balance of the PV Poisson-like operator (i.e., equal coefficients in the six directions). The level depths are computed iteratively as follows: first the grid uniformity is transformed into the equivalent form

$$\Delta z_k \Delta \overline{b}_k = f^2 \Delta x^2, \tag{10}$$

where Δz_k is the vertical thickness of a grid cell and is the associated buoyancy jump. Then, starting from equal values, the Δz_k values are modified iteratively until (10) is satisfied. Note that the well posedness of the PV inversion imposes a relationship between horizontal and vertical resolution through (10) that is often overlooked. In particular, a well-resolved deformation scale on the horizontal (e.g., $\Delta x = L_d/64$) should be accompanied with a corresponding vertical resolution (64 levels). We took care to always increase the resolution uniformly in the three directions. We define the nondimensional wavenumber $k_\Delta = L/\Delta x$ associated with the grid resolution. Table 1 summarizes all the scales defined so far and used hereafter.

TABLE 1. Summary of the wavenumbers used in the text: channel width k_0, forcing scale k_s, β scale k_β, deformation scale k_d, and horizontal gridsize scale k_Δ, given here for the highest resolution.

	k_0	k_s	k_β	k_d	k_Δ
Wavenumber	1	1.5	3	8	1024
Wavelength (km)	768	512	256	96	0.75

3. Linear stability analysis

Linear stability analysis of baroclinic instability is a well-covered subject. Here, the aim is simply to describe the properties of the reference jets because several features of the nonlinear turbulent regimes turn out to be rationalized with linear theory arguments.

We performed a numerical stability analysis of the linearized QG equations about the reference jet. The crucial quantity is the vertical profile of the jet meridional PV gradient

$$Q_y(z; \alpha) = \beta[1 - U^* \partial_{\tilde{z}} s + U^* s \delta(\tilde{z} - 1)], \tag{11}$$

where we consider its value in the middle of the channel [$F(0) = 1$]; $s = \partial_{\tilde{b}} G$ is proportional to the isopycnal slope; and the third term on the right-hand side (RHS) corresponds to the singular surface PV gradient (Fig. 2).

With the chosen criticality parameter ($U^* = 0.6$), the jet is indeed unstable because Q_y changes sign twice in the vertical. This is an expected property of an eastward surface-intensified jet for a Q_y that is positive at endpoints (the surface PV gradient is positive and the bottom PV gradient is $\beta > 0$, under the assumption of weak motions); consequently, it must change sign at least twice. The vertical location of these crossing points determines the nature of the regime (Charney versus Phillips) as well as the property of the growth rate, the critical levels, and the vertical structure of the unstable modes.

The growth rate $\sigma(k)$ is nonzero over a finite k range in the Phillips regime, whereas it extends over a semi-infinite interval in the Charney regime (Fig. 2). This difference accounts for much of the difference we will report later.

In the Charney case, there is no cutoff at large k; all the high wavenumbers are unstable. It is numerically challenging to compute as the eigenvectors get trapped to the surface as k increases. Practically we were unable to compute them beyond $k \sim 30$. This explains why the curve $\sigma(k)$ ends prematurely on Fig. 2. The asymptotic behavior is $\sigma \sim k^{-1}$, as $k \to \infty$ (Miles 1964). This property is due to the absence of a vertical scale associated with the Q_y sign reversal at the surface, because at the surface the two PV gradients (interior versus surface) are of opposite signs. The unstable modes are exponential-like on the vertical with a vertical scale decreasing as k increases. All the modes are surface intensified. Their vertical scale depends
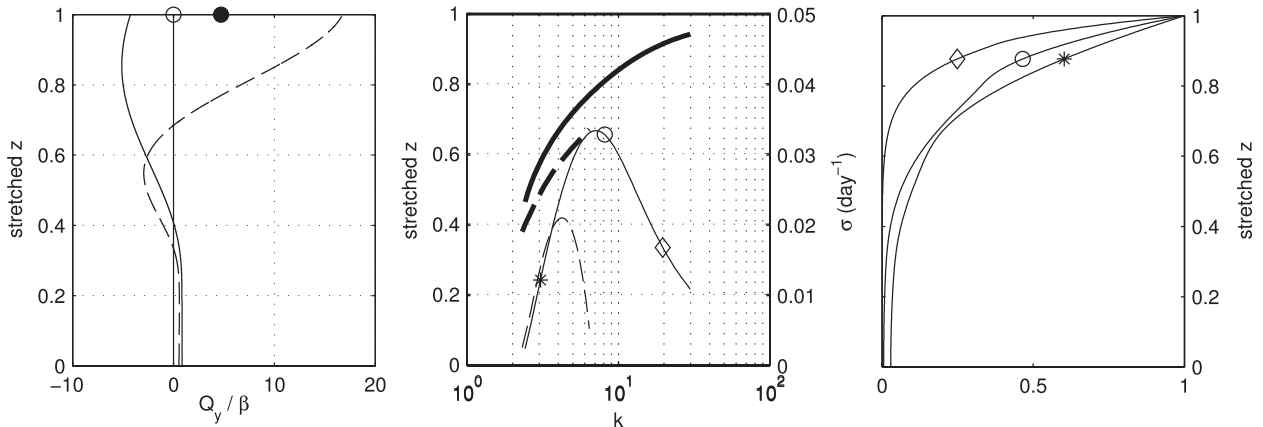
FIG. 2. (left) Vertical profile of the meridional PV gradient $Q_y(z)/\beta$ for the Charney (solid) and Phillips (dashed) cases, where the black and white circles indicate the surface PV gradient for the Charney and Phillips cases, respectively. (middle) Growth rate of the most unstable mode as a function of the wavenumber (thin line; right vertical axis) and corresponding critical level (thick line; left axis). (right) Amplitude of the most unstable modes corresponding to $k = 3$, 8, and 20 for the Charney case.

on k. For $k = 8$ (corresponding to a wavelength of L_d), the amplitude vanishes at the bottom. Because $k = 3$ emerges as a pivotal scale in the fully developed turbulent regime, we plot the structure of this mode. Contrary to shorter modes, it reaches the bottom.

In the two cases the critical level $z_c(k)$, where the phase speed $c(k)$ equals the jet velocity $c = U(z_c)$, corresponds to $Q_y < 0$. More precisely, for the smallest k unstable mode, z_c sits where Q_y first vanishes (moving upward); then, as k increases, z_c rises. For the Phillips case, the modes stop being unstable once z_c reaches the depth of the second Q_y zero crossing. For the Charney case, z_c increases and tends asymptotically to the surface as $k \to \infty$. Interestingly, the depth of the critical level for the most unstable mode is very close to the extremum of $Q_y < 0$, though it does not exactly coincide with it. There is definitively not a unique critical level in the studied regimes, and the picture of a pool of $Q_y < 0$ seems to be more appropriate.

The maximum growth rates have comparable magnitude, with the Charney case being slightly larger (Fig. 2), most likely associated with a larger $Q_y < 0$ extremum. The main difference between these two cases is the width of the unstable modes range: this causes the Charney case to be overall much more unstable. The linear instability at small scales for the Charney setup is readily seen during the spinup phase when the developing mesoscale meanders (also present in the Phillips problem spinup) are distorted by smaller features. Likewise, the presence–absence of small-scale activity is the primary difference observed between the Charney and Phillips steady states (see below). The results are consistent with Smith (2007), confirming that these idealized setups are not far from the real ocean.

We did not perform the linear stability analysis for the steady state, but the mean steady state should be less unstable, as suggested by the fact that the forcing tends to restore the pool of $Q_y < 0$ (section 4). Somehow, the mean state is less critical and closer to the marginal stability. However, BCI is active on a broad interval of modes (section 5), close to the interval predicted by the linear stability analysis of the reference jet. It seems unlikely the steady state is critical, in the sense of Green (1970), where there would be only one unstable mode, one critical level, and a vanishing growth rate.

4. PV properties

a. PV structure

Snapshots of PV (Fig. 3) reveal strong differences between the Phillips and Charney regimes, though the plotted variable is not the same (surface PV versus interior PV at surface). The Phillips case has fewer small-scale vortices than the Charney one, and it is evident that few-layer QG solutions resemble the Phillips solution, whereas the Charney solution bears some visual similarities with recent high-resolution PE simulations (Klein et al. 2008; Capet et al. 2008b). The eddies interact more strongly, and the turbulence zone has a larger extension in the meridional direction. In the vertical, finescale PV structures are also formed. The eddies seem to wrap the PV into paraboloid-like sheets (see the Charney case in Fig. 3 in the upper layers). A modal decomposition in the vertical would allow us to investigate the finescale dynamics associated with these features. As mentioned above, the classical decomposition into baroclinic modes is meaningless in the
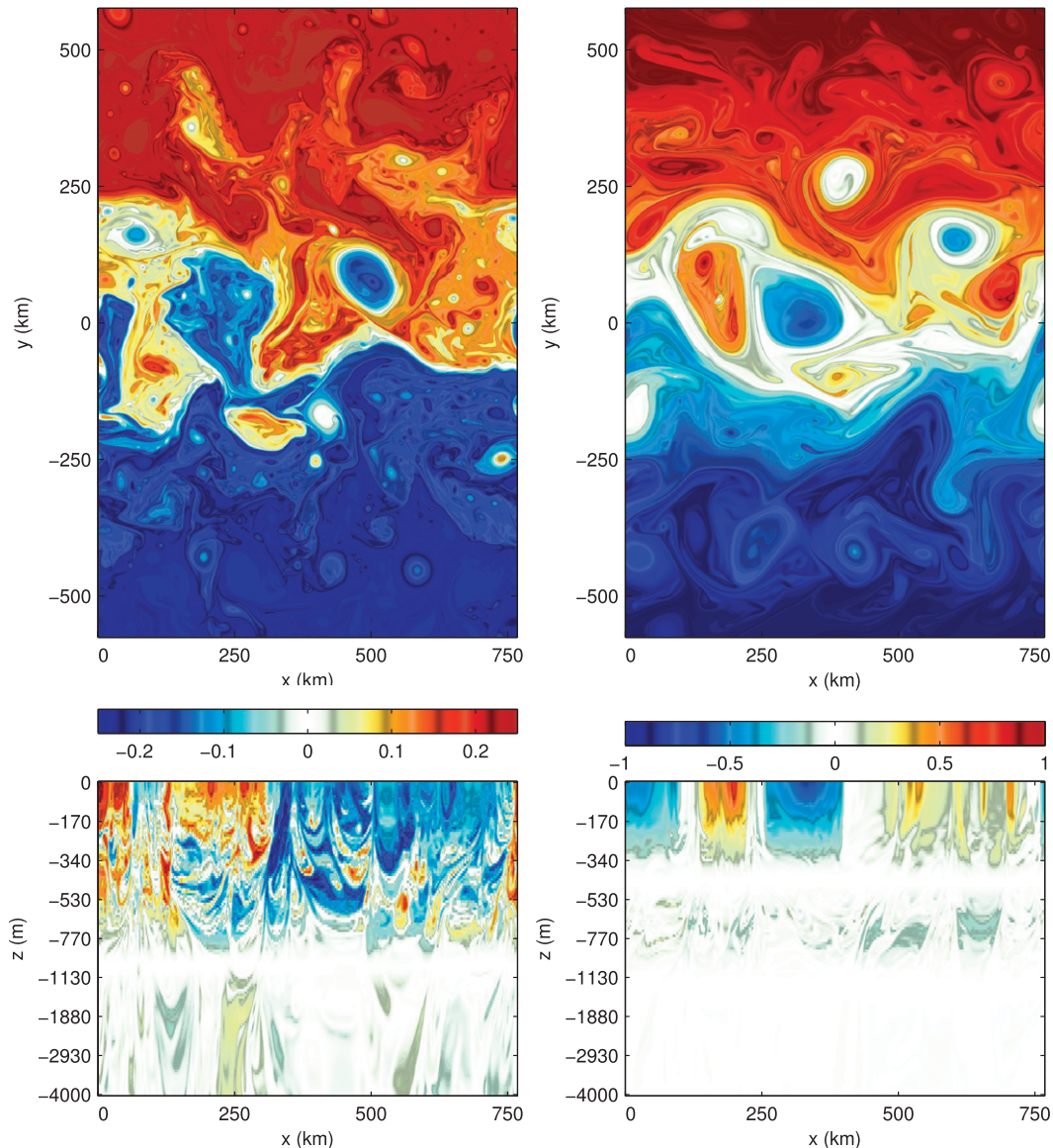
FIG. 3. Snapshots of (top left) surface PV, (top right) interior PV at surface, and (bottom) interior PV at $y = 0$ for (left) the Charney case and (right) the Phillips case.

presence of a surface PV sheet, where most of the small-scale PV variance is concentrated. We could not overcome this difficulty and do not elucidate the reasons behind the generation of turbulent structures with fine scales on the vertical. We only restrict ourselves to a (k, z) plane description that, nonetheless, has some valuable insight to provide.

b. PV forcing and small-scale dissipation

The PV forcing F_q of the experiment is quite different (Fig. 4). The vertical structure of the forcing is similar to the meridional PV gradient Q_y. In particular, the forcing is extremum where Q_y is extremum and vanishes at depths where $Q_y = 0$. Yet, the magnitudes of the extrema are larger at the depths where $Q_y < 0$ is extremum. The layers of $Q_y < 0$ seem to be more active, because there is a larger deviation from the reference state than the layers with $Q_y > 0$. The forcing pattern is relatively steady in time, with amplitude fluctuations up to 50% on time scales greater than weeks. The principal feature of the PV forcing worth noting is its quadrupolar structure. Each pole corresponds to an extremum of Q_y. In the Charney case, the poles are located at $z = -340$ m and in the surface PV. In the Phillips case, the poles are located at $z = -770$ m at the surface. The quadrupolar nature of the PV forcing is due to the BCI. To maintain a sustained
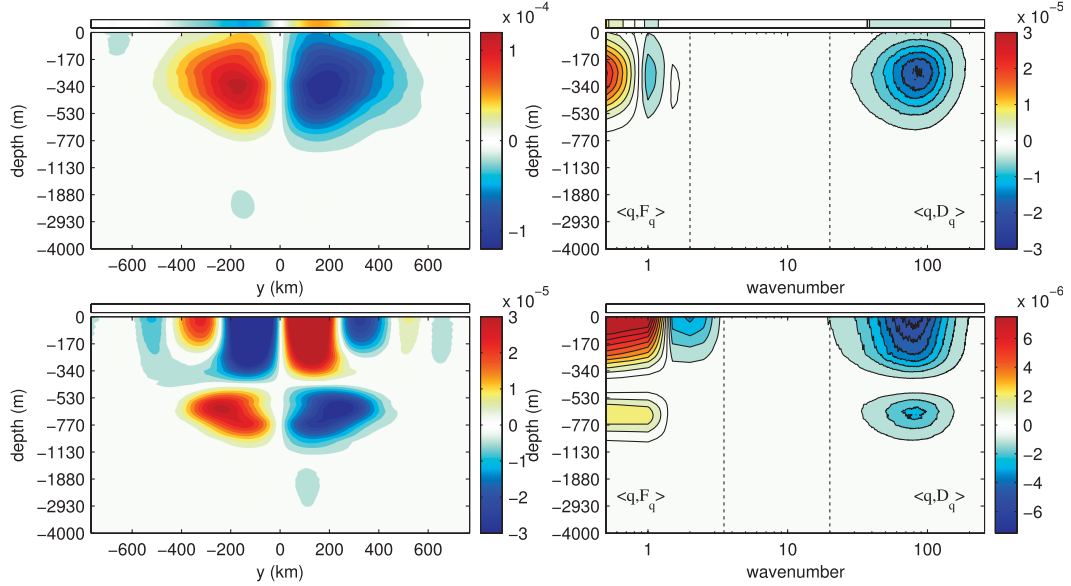
FIG. 4. Interior PV forcing F_q (and surface PV forcing; strip on top) for (top left) the Charney case and (bottom left) the Phillips case. Sum of forcing and dissipation of enstrophy in the semispectral plane (k, z) for (top right) the Charney case and (bottom right) the Phillips case. Dashed lines indicate where each term dominates.

BCI, the forcing has to impose a sustained quadrupolar PV anomaly, so that Q_y has a sign change in the vertical. The position of the upper dipole determines the nature of the flow: Charney when it sits in the surface PV and Phillips when it sits in the interior PV. The small-scale dissipation looks very different. It is highly intermittent in space and time; it tends to be concentrated along filaments while vast areas have weak dissipation. Note that the horizontally average of the sum of forcing and small-scale dissipation matches the enstrophy temporal derivative at each level (not shown), which confirms the soundness of the dissipation diagnostic.

c. Potential enstrophy budget

We now turn to the potential enstrophy budget in the (k, z) plane,

$$\underbrace{\langle q, J^*(\psi, q) \rangle}_{\text{I}} = \underbrace{\langle q, F_q \rangle}_{\text{II}} + \underbrace{\langle q, D_q \rangle}_{\text{III}}, \qquad (12)$$

where the bracket $\langle \cdot, \cdot \rangle$ denotes the horizontal cospectrum of the two variables averaged over 200 days. Here, we have assumed the time averaging period is long enough to cancel the time derivative term $\langle q, q_t \rangle$. Details of the cospectrum computation are given in appendix B. The terms (II) and (III) can be recognized as a source (if positive) or a sink (if negative) of potential enstrophy, whereas (I) connects the sources and sinks via nonlinear interactions. The sum of (I) over k vanishes as (I) only redistributes enstrophy across scales but does not create

nor destroy it. For the graphical representation (Fig. 4), each term $T(k, z)$ is multiplied by k to compensate for logarithmic shrinking. Indeed,

$$\int T(k, z)\, dk = \int T(k, z) k\, d(\log k) \qquad (13)$$

ensures equal areas of sources and sinks in log scale when their sum is zero. Without this compensation, the source–sink terms located at the largest scales would be several orders of magnitude greater than those at small scales even if they balance in an integral sense. All budget plots (involving cospectra) are compensated by k. Table 1 provides the correspondence between k and the dimensional space scale.

The forcing term (II) is mostly positive (red patch in Fig. 4). It is the source of enstrophy for the turbulence. The scale of injection is at the domain scale ($k = 0.5, 1$). The negative patch at $k \sim 2$ is also due to (II). It slightly decreases the net enstrophy input. The dissipation term (III) is negative everywhere (blue patch in Fig. 4). It is the sink of enstrophy. The dissipation scale k_{diss} (taken as the location of the core) follows the resolution $k_{\text{diss}} \approx k_\Delta/6.4$. Doubling the resolution simply shifts the blue patch by a factor of 2. The dissipation peak magnitude is unchanged when resolution increases, which indicates some form of convergence. Sources are located on the left of the figure (large scales), whereas dissipation is on the right (small scales). Figure 4 illustrates how enstrophy cascades downscale in geostrophic turbulence. Because the QG model allows no
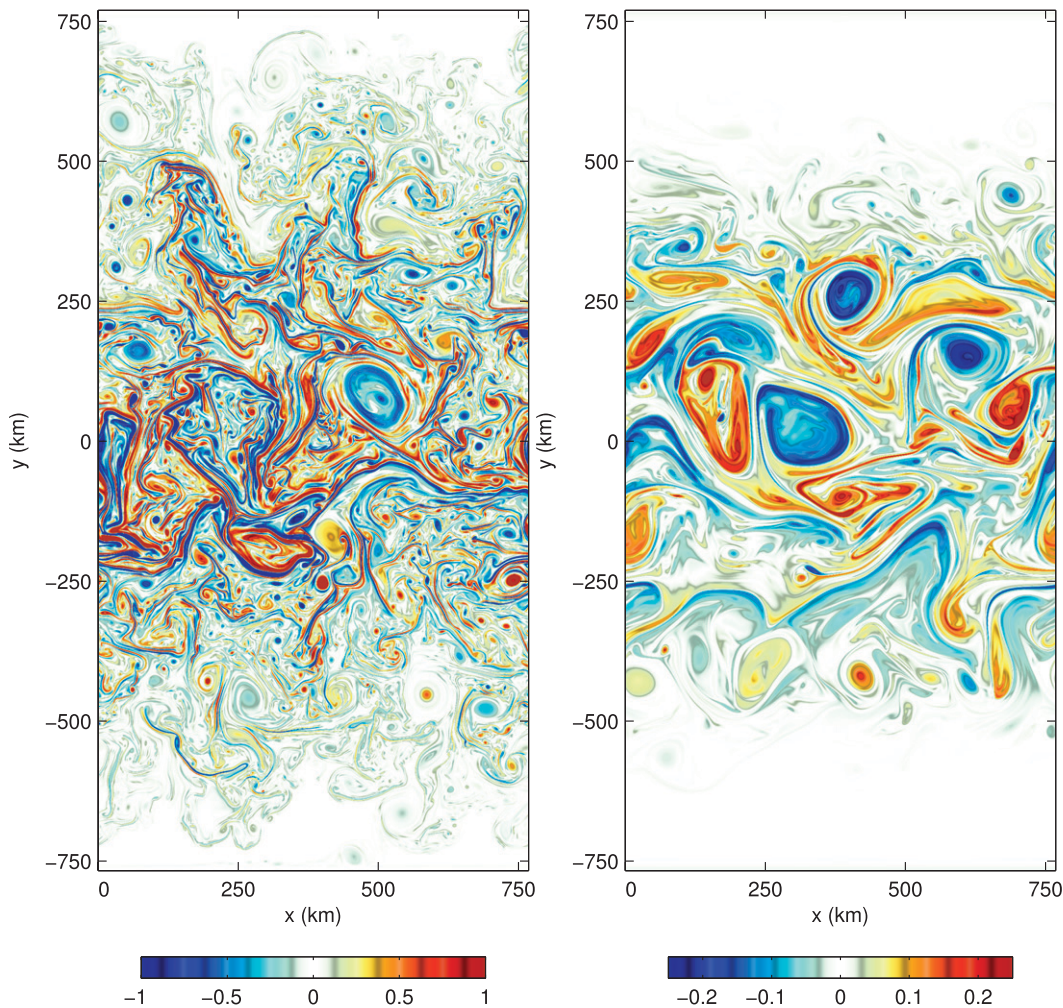
FIG. 5. Surface vorticity snapshot (ζ/f) at the statistical steady state for (left) the Charney case and (right) the Phillips case.

vertical PV flux (neither advective nor diffusive), the forward cascade occurs at every depth. This is consistent with the fact that PV obeys a tracer advection equation. The enstrophy forcing is sharply peaked at the basin scale because of the forcing procedure. Dissipation and forcing scales are well separated at this resolution ($k_\Delta = 512$). Consequently, there are almost two decades of quasi-inviscid dynamics (and more than two for $k_\Delta = 1024$).

d. Vorticity

Surface vorticity snapshots dramatically differ between the two regimes (Fig. 5). The Charney case is finer grained with lot of submesoscale structures. In comparison, the Phillips case looks smoother. In the Charney case, high values of vorticity tend to be in the fronts rather than in the eddies. As the resolution increases, the vorticity extrema increase in filaments because nothing prevents it. This is not surprising as the ageostrophic circulation has

been shown to be important in the balance of filaments (McWilliams et al. 2009). This is confirmed by the probability density function (PDF) of vorticity at the surface (Fig. 6). It has a marked exponential-law behavior for both side of the PDF: $P(\zeta) \sim \lambda \exp(-\lambda|\zeta|)$, with λ a parameter that depends on depth and the regime. The Phillips case exhibits a steeper PDF than Charney's case (as can be anticipated from vorticity snapshots in Fig. 5), and this difference becomes more dramatic as the resolution increases. The PDF of the Phillips case shows almost no dependency on the resolution, but the one for the Charney case shows no sign of convergence near the surface. In fact, λ almost linearly scales with resolution ($\lambda \sim \Delta x$), and extrapolating this tendency for infinite resolution would yield a flat PDF for vorticity at surface. Clearly near-surface submesoscale processes escape a QG description. The Charney case does resemble equivalent PE simulations (Klein et al. 2008). The stirring is very
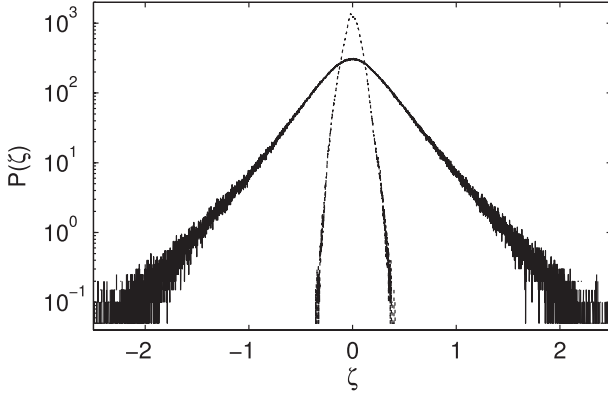
FIG. 6. PDF of surface vorticity (ζ/f) for the Charney case (solid) and the Phillips case (dotted). Resolution is 512 ($\Delta x = 1.5$ km).

intense; the bigger eddies hardly get circular because the deformation is too strong.

5. Energetics

a. Momentum and buoyancy equations

The QG Eqs. (1)–(3) can be written equivalently in terms of momentum ($u = -\psi_y$, $v = \psi_x$), geostrophic velocity, and buoyancy equations ($b = f\partial_z\psi$),

$$\partial_t u + J(\psi, u) = +fv_a + v\beta y + F_u + D_u + E(u), \quad (14)$$

$$\partial_t v + J(\psi, v) = -fu_a - u\beta y + F_v + D_v + E(v), \quad (15)$$

$$\partial_t b + J(\psi, b) = -N^2 w_a + F_b + D_b, \quad \text{and} \quad (16)$$

$$0 = \partial_x u_a + \partial_y v_a + \partial_z w_a, \quad (17)$$

where (u_a, v_a, w_a) are the three components of the ageostrophic velocity. Here, $F_{u,v,b}$ and $D_{u,v,b}$ are the forcing and the dissipation of momentum and buoyancy, respectively, connected to the PV forcing. They are thus more easily comparable to PE. The boundary conditions are no flux for both geostrophic and ageostrophic velocities. The KE and APE spectral densities (spectra for short) are

$$\text{KE} = \frac{\langle \mathbf{u}, \mathbf{u} \rangle}{2} \quad \text{and} \quad \text{APE} = \frac{\langle b, b \rangle}{2N^2}, \quad (18)$$

where $\mathbf{u}$ denotes the geostrophic velocity vector (u, v). The KE budget is given by the cospectrum of $\mathbf{u}$ and the momentum equations,

$$\underbrace{\langle \mathbf{u}, J(\psi, \mathbf{u}) \rangle}_{\text{NLK}} = \underbrace{-\partial_z \langle \psi, w_a \rangle}_{P} + \underbrace{\langle w_a, b \rangle}_{C}$$
$$+ \underbrace{\langle \mathbf{u}, \mathbf{F_u} \rangle}_{\text{FK}} + \underbrace{\langle \mathbf{u}, \mathbf{D_u} \rangle}_{\text{SDK}} + \underbrace{\langle \mathbf{u}, \mathbf{E(u)} \rangle}_{D}, \quad (19)$$

where we have used (17). The APE budget is given by the cospectrum of b/N and the buoyancy equation

$$\underbrace{\langle N^{-2}b, J(\psi, b) \rangle}_{\text{NLA}} = \underbrace{-\langle w_a b \rangle}_{C} + \underbrace{\langle N^{-2}b, F_b \rangle}_{F}$$
$$+ \underbrace{\langle N^{-2}b, D_b \rangle}_{\text{SDA}}, \quad (20)$$

where again we have assumed that the time averaging is long enough to make the time derivative terms vanish. As for the enstrophy budget, NLK and NLA are responsible for energy transfers across scales. Here, P is the pressure work; it is responsible for the vertical energy transfer. It can be seen as the divergence of the vertical energy flux $\langle w, \psi \rangle$; C is the conversion from APE to KE; FK and SDK are the forcing and small-scale dissipation of KE; D is the dissipation of KE through bottom drag; and F and SDA are the forcing and small-scale dissipation of APE.

b. The gauge issue

The forcing and small dissipation terms in (14)–(16) are defined up to a certain gauge that is crucial to elucidate because this ambiguity impacts the energy budgets. Two different gauges yield two different buoyancy forcing F_b and therefore two different APE forcings F. The gauge issue arises because the interior PV is basically the 3D divergence of ($v, -u, fN^{-2}b$). Consequently, F_q is related to $F_{u,v,b}$ through $F_q = \nabla \cdot \mathbf{F}$, where $\mathbf{F} = (F_v, -F_u, fN^{-2}F_b)$. Because the numerical QG model is solved for PV, we only have access to F_q (i.e., the divergent part of $\mathbf{F}$). The rotational part of $\mathbf{F}$ is unknown because it has no signature on F_q. The PV equations are invariant under the change $\mathbf{F} \to \mathbf{F} + \nabla \times \mathbf{G}$, where $\mathbf{G}$ is the gauge vector. Boundary conditions impose restrictions on the gauge but only at the boundary. The momentum–buoyancy forcing is thus underdetermined. The same holds for the small-scale dissipation.

Depending on the gauge, the forcing can be a pure momentum forcing (without any buoyancy forcing) or the contrary or any combination between these two extremes. The gauge also changes the ageostrophic circulation: because a gauge change leaves the solution unchanged, only the terms that involve ageostrophic velocity in (14)–(16) are able to balance the gauge change. A given forcing $\mathbf{F}$ can thus be split in two parts: a divergent part, forcing the PV and the geostrophic circulation, and a rotational part, forcing an ageostrophic circulation. Because QG energy budgets only involve the geostrophic velocities, we decided to retain in $\mathbf{F}$ only the part that forces the geostrophic circulation. This sets the gauge. The forcing $\mathbf{F}$ has no rotational component; therefore, it derives from
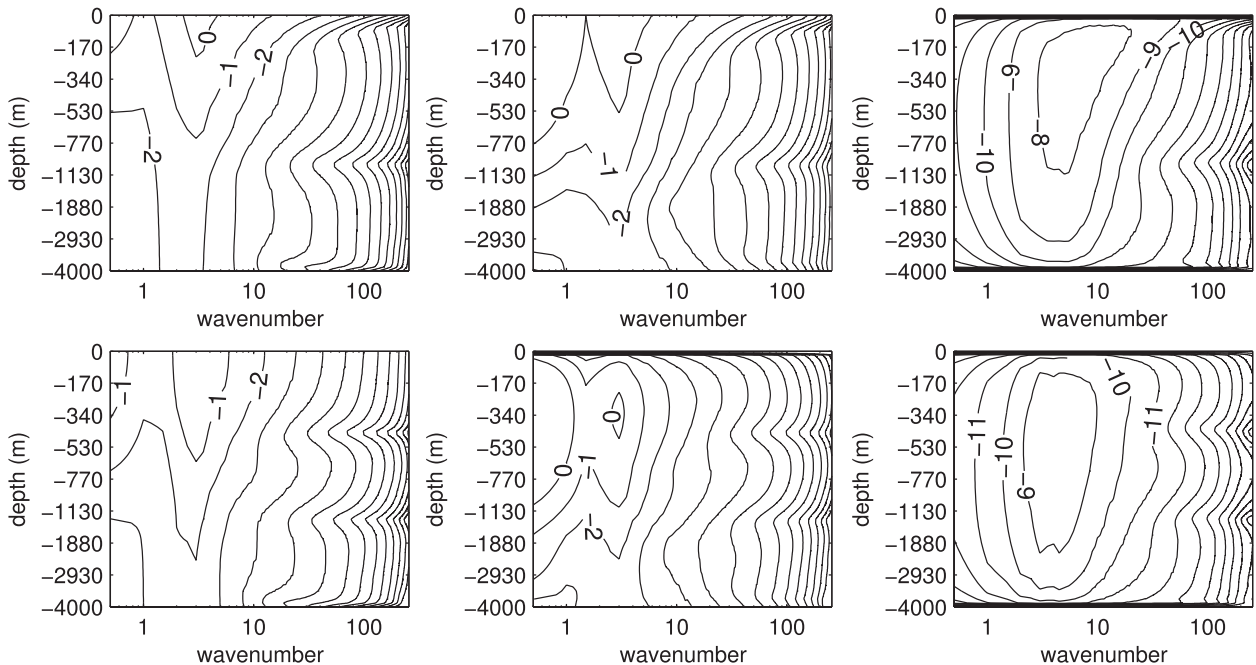
FIG. 7. The $\log_{10}$ of (left) KE, (middle) APE, and (right) vertical KE spectra for (top) the Charney case and (bottom) the Phillips case.

a potential Φ: $\mathbf{F} = \nabla\Phi$. In practice, Φ is computed by inverting the PV operator with $(q, b, \Delta\Gamma)$ replaced by $(F_q, F_b, 0)$ (appendix B). The same procedure is applied for the small-scale dissipation terms. The resulting forcing is dominated by the buoyant contribution with $F_q \approx \partial_z(fN^{-2}F_b)$ and a marginal contribution from (F_u, F_v). The buoyancy forcing F_b (not shown) may be deduced by integrating F_q on the vertical. It is surface intensified and has a dipolar structure in y with the forcing tending to heat up the warm side of the channel and to cool down the cold side (not shown).

c. Spectra

We begin the study of the energetics by first investigating the properties of KE and APE spectra in the (k, z) plane (Fig. 7). Overall the spectra look very similar. The peak is located at $k \sim 3$. The physical interpretation will be clear when looking at the energy budgets. Below 1000-m depth, the spectra are very uniform in z, except at the bottom (where a bottom mode develops because the bottom drag creates a PV sheet there) and at the scale of arrest (where the KE spectrum has a net decrease from 1000 m down to the bottom). In the Charney case, the spectra have a shallow tongue of high energy level close to the surface. This is the signature of the surface mode that tends to develop exponential structures over the vertical (Held et al. 1995). This tongue is totally absent in the Phillips case. The APE is even zero at the surface, because there is no surface buoyancy. The shallowest

spectra are found at surface, in the Charney case. They are more compatible with k^{-2}, as also found by Capet et al. (2008b) and Klein et al. (2008), than with the $k^{-5/3}$ arising in pure surface QG dynamics (Capet et al. 2008a). Blumen (1978) predicted such an intermediate regime when both interior and surface PV compete. An interesting spectrum is the vertical KE $\langle w, w \rangle/2$ (Fig. 7). It should be noted that this quantity can be diagnosed but is not involved in the energy budget. It can be created or destroyed at no energetic expense, a property that comes essentially from the hydrostatic assumption and hence is also shared by PE systems. The comparison between the two regimes is dramatic. The differences mainly concern the upper 1000 m, the mesoscale, and the submesoscale, where vertical KE is much stronger in the Charney case than in the Phillips case. This confirms Klein et al. (2008) finding that including surface PV dynamics not only energizes the submesoscale at the surface but also intensifies the vertical motions in the pycnocline at larger scales.

d. Budgets in the (k, z) plane

We present first the APE budget (Fig. 8). APE is created by two terms: the forcing F at large scale ($k < 3$) and the conversion C at the scale of $k \sim 3$ that converts KE to APE. The first term is an external source, and the second is an internal source. This is new because, in the classical picture of geostrophic turbulence energetics (Salmon 1980), APE is only forced externally. APE is depleted and converted to KE by the term C at scales where $k > 3$.
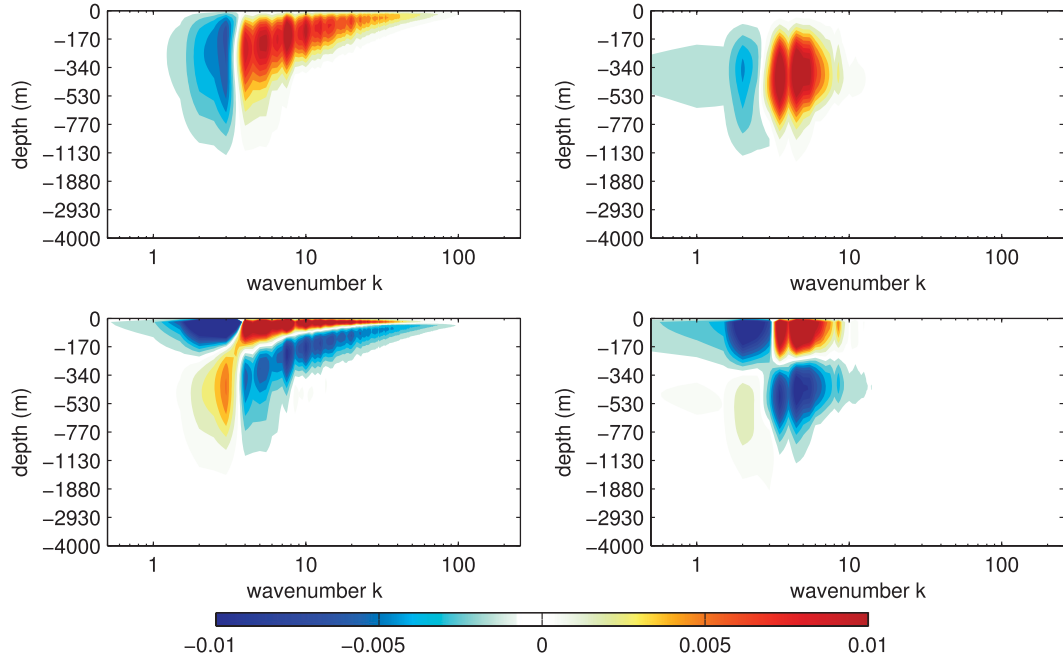
FIG. 8. (top) Conversion term $C = \langle w, b \rangle$ and (bottom) divergence of the vertical energy flux $\partial_z \langle w, \psi \rangle$ for (left) the Charney case and (right) the Phillips case. Terms are multiplied by the wavenumber k to compensate for the logarithmic shrinking. The horizontal resolution is 512 ($\Delta x = 1.5$ km).

The area in the (k, z) plane where $C > 0$ depends on the regime. It is the signature of BCI in the fully developed regime and surprisingly the location where $C > 0$ is in good agreement with the prediction of the linear stability analysis: for the Charney regime, the conversion occurs at all scales but gets shallower as k increases; in the Phillips regime, only a limited interval of k, close to k_D, participates in the conversion. Yet, the scale at which C is maximum is not the scale of the most unstable mode (see Fig. 2). Moreover, the scale of the most unstable mode does not seem to play any particular role. Because the sources of APE are on the left of the diagram and the sinks are on the right, APE has a forward cascade. Note also that, contrary to KE, there is no vertical transfer of APE. In particular, the APE created close to the surface in the Charney regime can only be converted into KE at very small scales. The closer to the surface the APE is injected, the harder it is for the BCI to convert it to KE. Overall, the dissipation of APE is very small, meaning that almost all the APE source is converted into KE at some scale.

The KE budget is very different. The forcing term (III) is very small, several orders of magnitude smaller than the APE forcing F. Hence, there is no direct source of KE; KE is only created internally via $C > 0$ at scales $k > 3$. BCI is therefore the ultimate process generating motions. In pictorial word BCI is the engine of the turbulence. KE is depleted by essentially two terms: $C < 0$ and the bottom

drag D term, with both of them acting mostly at $k \sim 3$. The location of the sources and the sinks are reversed with respect to APE; therefore, KE has an inverse cascade. Note that this inverse cascade prevails at all scales, including the submesoscale. This is a QG property that is no longer true in a PE model (Klein et al. 2008; Molemaker et al. 2010). This (k, z) view of the energetics also reveals the role played by the pressure work P or equivalently the vertical energy flux $\langle w, \psi \rangle$ on the vertical transfers. This flux is very well correlated with C. In particular, it is upward where $C > 0$ and downward where $C < 0$ and has the same location as C. The upward branch is associated with the BCI. The conversion of APE to KE at depth is systematically fluxed upward. Consequently, the motions near the surface are energized at scales $k > 3$, whereas motions beneath the core of $C > 0$ are not energized at all. At the scale $k \sim 3$ where $C < 0$, the flux is downward and reaches the bottom. At this scale, the whole water column is set into motion, which allows the bottom drag to be effective. The bottom dissipation mainly occurs at this scale. This downward flux can be interpreted as the tendency for barotropization, though the flow is still largely surface intensified at $k \sim 3$.

The emerging picture of this analysis is largely compatible with the classical one (Salmon 1980), although it differs by two important aspects. The first one concerns the vertical aspect. Because the turbulence is fully resolved in the vertical and because the surface buoyancy
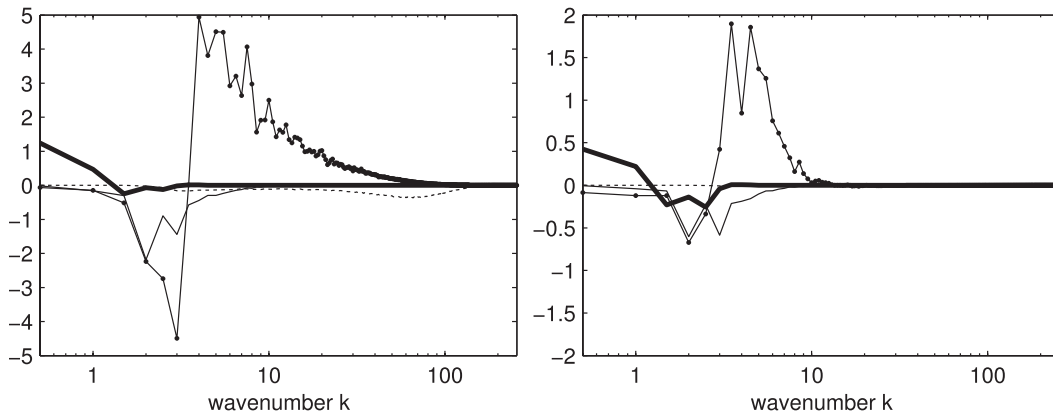
FIG. 9. Depth-integrated energy budgets for (left) the Charney case and (right) the Phillips case: APE forcing (thick), conversion term C (solid with circles), bottom dissipation (thin), and sum of KE and APE small-scale dissipation (dotted). All the terms are multiplied by k to compensate for the logarithmic shrinking.

prevents the use of a decomposition into vertical modes, baroclinic and barotropic energies have been replaced by APE and KE. The exchange of energy between vertical modes at a given scale k is rephrased in terms of vertical energy flux $\langle w, \psi \rangle$. This flux is systematically correlated to the conversion term C. The second novelty shown by this study is the existence of an internal energy loop in the energetics. The APE is converted into KE by BCI ($C > 0$). KE cascades backward up to the scale of arrest $k \sim 3$, where a large fraction is converted back into APE ($C < 0$); the remaining is fluxed downward to the bottom where it is dissipated. The mechanism by which $C < 0$ at $k \sim 3$ is discussed in Larichev and Held (1995). The meridional fluxes of both PV and heat are realized by the largest eddies: that is, at $k \sim 3$ (see next section). These fluxes are downgradient; consequently, vb negatively correlates with the meridional gradient b_y, yielding $\langle b_y, vb \rangle < 0$. This term is the dominant part of the nonlinear transfer in Eq. (20) because $\langle b, J(\psi, b) \rangle \sim \langle b, (vb)_y \rangle = -\langle b_y, vb \rangle$. At this scale, the main APE balance reads $N^{-2} \langle b_y, vb \rangle \sim$ to the term C; thus, $C < 0$. The presence of $C > 0$ at the scale of arrest is responsible for this internal energy loop. The amount of energy processed by the BCI is larger than the energy put in by the forcing. This loop is a robust feature of the two investigated regimes. Its existence is independent of the surface PV. To our knowledge, this is the first time a study reports on this loop.

The differences between the two regimes are twofold: (i) C is larger in the Charney case and (ii) $C > 0$ is sharply localized in spectral space for the Phillips case, whereas it is unbounded for the Charney case. In this latter case, there is a conversion from APE to KE at all scales. All scales shorter than the deformation radius are energized by the BCI. This energization is responsible for the shallowness of the KE spectrum near the surface

and explains the difference in patterns of both PV and vorticity at surface (Fig. 3). When the control parameter α is varied, the qualitative change of regimes is in broad agreement with the prediction of the linear BCI analysis: when $Q_y < 0$ is purely interior, the surface PV gradient and Q_y in the upper layers are both positive and the regime is more Phillips-like. When $Q_y < 0$ hit the surface, the regime becomes Charney-like. It worth emphasizing that the Phillips regime is not incompatible with isopycnal outcropping. The chief ingredient is not the presence of surface PV in itself but the vertical location of the pool of negative Q_y.

e. Depth-integrated budgets

Consider now depth-integrated budgets (Fig. 9). The forcing consists basically of APE forcing because KE forcing is negligible. The dissipation is done by three terms. Their spectral signature is dramatically different. Ekman drag mostly acts around the scale of arrest ($k = 2, 3$). However, the inverse cascade of KE is not completely stopped and continues until it reaches the largest scales. We introduce ϵ the fraction of dissipation that occurs for $k < 2$. It is on the order of 10% (Table 2). The small-scale dissipation is weaker and at small scales, and it vanishes in the Phillips case. More importantly, the forcing and Ekman drag do not depend on the resolution of the model, whereas the small-scale dissipation does. We checked the same budget for twice the resolution (1024): the dissipation peak is shifted by a factor of 2, and its magnitude is divided by 2. This means that the small-scale dissipation is acting only because there are not enough scales resolved. In the limit of infinite resolution, the total input of energy should be dissipated at the scale of arrest by the Ekman damping. This confirms that QG physics is unable to perform a forward cascade

TABLE 2. Volume-integrated conversion rates (after applying a factor 10^3). The ratio $\eta = C_+/F$ is the efficiency of the energy cycle, and ϵ measures the part of KE that leaks to k smaller than $k = 2$. The dissipation rate $|D|$ is equal to the forcing term F.

Experiment	F	C_+	η	ϵ
Charney	2.90	9.65	3.32	0.14
Phillips	0.89	2.23	2.50	0.11

of total energy (Molemaker et al. 2010; Capet et al. 2008a). Nevertheless, we should stress that QG does exhibit a forward cascade of APE, as we have shown, but this APE is entirely converted into KE and fluxed backward at larger scales. The net result is that the total energy (sum of APE and KE) is not cascading at all apart from the cascade from the forcing scale to the scale of arrest. Still, the connection between the source (forcing at surface) and the sink (Ekman drag at bottom) is far from trivial because energy has to cascade forward in APE form before it is converted to KE at some scale. The vertical connection is important too, because the APE cascade dominates in the interior while KE cascade dominates at the surface. The pressure field is responsible for carrying the energy upward (at small mesoscale and submesoscale) and downward to the bottom at the scale of arrest.

The energy cycle is also manifest in this budget. It is now possible to quantify it. Let us split the APE to KE conversion term in two terms, $C = C_+ + C_-$, where $C_+ = (C + |C|)/2$ is the net conversion of APE to KE ($C_+ > 0$) and $C_- = (C - |C|)/2$ is the net conversion of KE to APE ($C_- < 0$) (Table 2). It is important to realize that the forcing F is smaller than $|C_+|$ because basically $C_+ = |C| + F$. The efficiency of the forcing $\eta = C_+/F$ measures this amplification factor. It is larger (3.3 versus 2.5) for the Charney case than for the Phillips case but by a smaller factor than between the forcings (2.9 versus 0.9). A schematic of this energy cycle is given in Fig. 10.

f. Volume-integrated budgets

The energy cycle can be coarsen further into a four-box summary (a Lorenz view) where the two forms of energy (KE and APE) are split into a mean and an eddy component with transfers depicted as arrows connecting these boxes. The classical way to separate between mean and eddy is to average temporally and zonally. We have chosen to depart from this. The mean and the eddy parts are defined on a spatial scale argument. To that purpose, a cutoff scale k_c is introduced. The mean corresponds to $k \le k_c$, and inversely the eddies correspond to ($k > k_c$). It is logical to include the scale of arrest in the eddy part, because this is the scale where the eddies transport the PV. We thus chose $k_c = 1.5$ (corresponding to $L = 512$ km). Note that the classical zonal time mean slightly leaks
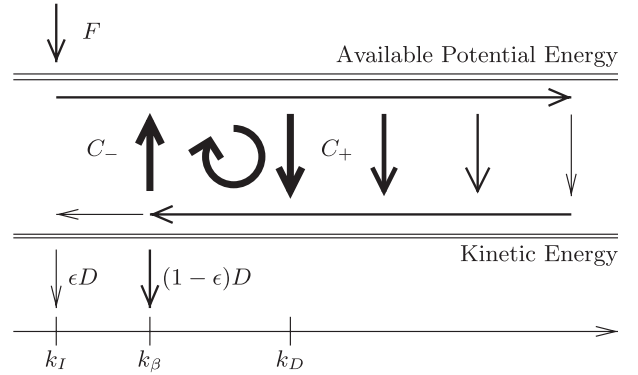

FIG. 10. Schematic of the energetics: the forcing F inputs APE at the largest scale. APE cascades forward to smaller scales where it is completely converted to KE (C_+) at the deformation scale k_D (for the Phillips case). At smaller scales (for the Charney case), KE cascades backward up the scale of arrest (k_β), where the main fraction is converted back to APE (C_-) and the other part is dissipated at bottom through Ekman friction (D). Part of KE (ϵD) cascades beyond the scale of arrest and is dissipated at larger scale. In this schematic, $F = |D|$ and $C_+ = |C_-| + F$. In Salmon's (1980) schematic, C_- is absent, so $F = |D| = C_+$. In Larichev and Held (1995), C_- is assimilated to the external forcing, but it does not convert KE to APE; there is no energy cycle.

into the $k > k_c$ range. The energy partition among the four boxes is given in Table 3. With these definitions, the energy is input by forcing in the mean state. The forward cascade of APE is responsible for the transfer of mean APE into the eddy APE (EAPE). The energy cycle is distorted as the conversion term from EAPE to EKE is smaller than it is really because it is the net conversion term (including the conversion from KE to APE at the scale of arrest). Bottom dissipation mainly occurs in the EKE reservoir, although there is a slight leakage (a small percent) of EKE into the mean KE reservoir where it is bottom dissipated. The whole energy cycle is illustrated in Fig. 11. This box picture is interesting; it is a kind of minimalist view. Its main drawback is oversimplification of reality, especially in completely hiding the energy loop. Underlying these averaged values, EKE and EAPE fluctuate in time with an rms to mean ratio of 10% and a dominant period of roughly 3 months.

g. Scale of arrest

There are basically two processes that can set the scale of arrest $k_0 = 3$ (corresponding to $L = 256$ km): the bottom friction or the β effect. They both can be understood in terms of PV dynamics. At the scale of arrest, there is a qualitative change in the PV dynamics. On one hand, the friction argument states that bottom friction becomes a leading-order process, competing with the advection of PV. This yields a friction scale $L_\lambda = U_\lambda$. On the other hand, the β effect argument states that the PV

TABLE 3. Volume-integrated KE and APE (10^3 cm^5 s^{-2}) after distinguishing mean ($k \le k_c$) and eddy ($k > k_c$), where $k_c = 1.5$.

Experiment	MAPE	MKE	EAPE	EKE
Charney	15.0	0.19	7.83	3.49
Phillips	13.6	0.13	2.28	1.45

dynamics transforms into a wavelike regime at this scale, where βv balances the advection of PV anomaly. This yields the so-called Rhines scale $L_\beta = \sqrt{U/\beta}$. Taking $U = 0.1$ m s^{-1} for the typical zonal-jet velocity, these scales are $L_\lambda \approx 850$ km and $L_\beta \approx 80$ km. At this stage, both processes remain basically acceptable candidates to explain the scale of arrest (with an ad hoc prefactor). However, a scaling is by no mean a proof. Basically, we want to know which of these processes sets the scale of arrest. To settle the issue, we repeat the Charney experiment with a friction 4 times greater (corresponding to a restoring time of 25 days) and with all other parameters unchanged. The result is striking: the forcing is unchanged; the surface spectra are unchanged; and even the integrated dissipation is unchanged. The scale of arrest is exactly the same. The only change is the magnitude of the bottom velocity: it is 4 times smaller. We also checked that for reduced bottom friction; the scale of arrest is unchanged too. We conclude that the scale of arrest is given by the Rhines scale (although a π prefactor, $L_\beta = \pi\sqrt{U/\beta}$, gives a better estimate), and so it is the scale at which the eddies stop being coherent and transform into wavelike structures. In retrospect, this can be seen in the snapshots for PV (Fig. 3) where the largest coherent structures have roughly this scale, though they are already affected by the wave dynamics and they do not last very long. This sensitivity experiment also reveals that the dissipation is completely enslaved to the forcing. The effect of friction is not to set the value of the dissipation but to determine the intensity of the bottom velocity. The integrated dissipation adjusts to the forcing. This is seemingly in contrast with biperiodic, two-layer QG turbulence for which the intensity of the turbulence is generally sensitive to the magnitude of the bottom friction coefficient (Thompson and Young 2006).

6. Eddy fluxes

Because of the high resolution of these experiments, there is a wide gap in scale between the forcing and the dissipation. Consequently, the eddy dynamics is fairly clean and allows a clear exposition of their roles in the mean state balance. The central quantity for this is the meridional eddy PV flux $\overline{vq}$. We first describe it, in physical space and in scales. We see how it is related to the large-scale PV gradient, thereby investigating the eddy
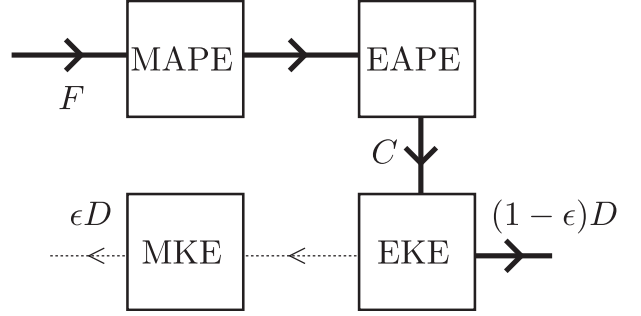

FIG. 11. Energy cycle in the four-box summary: the mean energies, MAPE and MKE (the eddy energies, EAPE and EKE), are defined as $k \le k_c$ ($k > k_c$). The dissipation of MKE (ϵD) is very small compare to dissipation of EKE $(1 - \epsilon)D$. The energy cycle is completely hidden in this schematic.

diffusivity. Then, we consider it divergent from the Eliassen–Palm fluxes and describe the latter. Last, we provide the transformed Eulerian mean view of the experiments and elucidate the gauge problem mentioned in section 5.

a. PV eddy diffusivity

The use of an explicit PV forcing allows us to identify it with the divergence of the meridional PV flux $\overline{vq}$. Indeed, the zonal- and time-averaged (overbar) PV equation is

$$\partial_y(\overline{vq}) = \overline{F}_q + \overline{D}_q. \tag{21}$$

The diffusive term vanishes because it does not contribute at large scale. Thus, we are left with

$$\overline{vq} = \int_{Ly/2}^{y} \overline{F}_q \, dy. \tag{22}$$

The PV eddy flux $\overline{vq}$ is directly linked to forcing and connects the source of PV (where $F_q > 0$) to the sinks (where $F_q < 0$) (Fig. 4). This relation emphasizes the importance of the experimental design: the form of the prescribed forcing directly shapes the eddy PV transport. In these experiments, the eddy PV transport is not an internal degree of freedom; it is totally prescribed from start. Therefore, the choice of the forcing structure is crucial in any kind of experiment like this.

Because the forcing is smoothed by construction, the PV eddy flux is also a smooth field, at least after zonal and temporal averaging. Its meridional structure is the same for the three experiments, whereas its vertical structure depends on the reference PV profile (Fig. 2): it is zero where Q_y vanishes (because the PV is uniform so it cannot be transported) and extremum where Q_y is extremum.
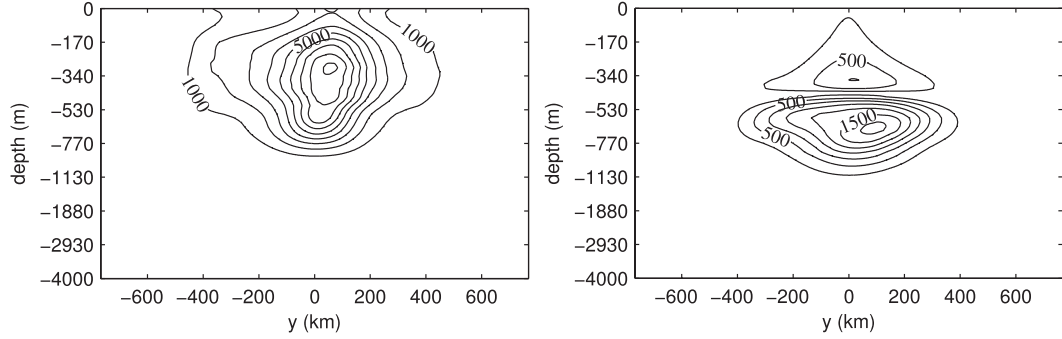
FIG. 12. Eddy PV diffusivity (in $m^2\,s^{-1}$) for (top) the Charney case and (bottom) the Phillips case.

Obviously, it is tempting to relate this PV eddy flux to Q_y and check an eddy diffusivity κ. We have computed κ by 1) averaging zonally and in time the PV field $\overline{q}$; 2) taking the meridional gradient; and 3) using a practical definition that allows dealing with a zero denominator, basically $\kappa = \mathrm{sgn}(\overline{q}_y)\overline{vq}/(\overline{q}_y^2 + \epsilon)^{1/2}$, with ϵ being a small value. Interestingly, this eddy diffusivity is highly nonuniform (Fig. 12) but has a simple structure. In particular, it is positive everywhere, showing the eddy flux is downgradient. The diffusivity is relatively weak where the PV gradient is in the same direction as β. The diffusivity is a maximum where the PV flux is both maximum and opposite of the planetary PV gradient β. The location of this maximum could be arguably attributed to the presence of a critical layer responsible for enhanced diffusivity (Green 1970; Killworth 1997; Smith and Marshall 2009). Likewise, the strong correlation between region of $Q_y <$ 0 (Fig. 2) and the maximum diffusivity supports the idea that eddies are the relaxing process in the BCI, and their effectiveness is at a maximum where there is something to relax. At the least, this interior location is incompatible with the theory predicting a maximum diffusivity where EKE is maximum. It is worth noting the peak value for the diffusivity is partly explained by a mixing length argument, $\kappa = v_{rms}L_{mix}$, where v_{rms} is the rms velocity and L_{mix} is a mixing length. Based on the spectral analysis of vq, we chose $L_{mix} = 250$ km (corresponding to $k = 3$). We found $\kappa \approx 40\,000$ $m^2\,s^1$ for the Charney case and $\kappa \approx 15\,000$ $m^2\,s^{-1}$ for the Phillips case. This model overestimates the peak value by a factor of 4 but is able to explain the difference between the two regimes (Charney diffusivity is threefold larger). The direct estimate for diffusivity ($\kappa \approx 10^4$ $m^2\,s^{-1}$ for the Charney regime) (Fig. 12) is smaller and in agreement with recent estimates of PV diffusivities (up to $\approx 5 \times 10^3$ $m^2\,s^{-1}$) in the SO (Smith and Marshall 2009). Overall, we think these results are an interesting experimental point in the quest for deriving a theory that explains the diffusivity. They support the steering level argument though in these experiments

there is not a particular steering level but a vertical interval of critical levels associated with a range of unstable modes. In the end, the depths of both the diffusivity maximum and the PV forcing maximum match the location of the pool of negative Q_y, which also coincide with the location of critical levels.

b. $\overline{v'q'}$ in (k, z) space

Another way to describe the meridional PV flux is to look at its signature in the (k, z) plane: namely, by plotting the cospectrum $\langle v, q \rangle$ (not shown). The vertical structure depends on the regime. More interestingly, it is sharply peaked around $k = 3$ in the two regimes. These scales are larger than the deformation radius ($k = 8$) and correspond to the scale of arrest k_0 for the cascade of KE. We discuss this scale in the next section. However, it is a confirmation of the Larichev and Held (1995) central result, "the eddy PV flux is localized at the greatest scale to which inverse KE cascade extends." Therefore, switching from the Charney to the Phillips case only changes the vertical structure, not the scale at which the transport occurs. The smaller eddies, although very intense and very numerous in the Charney case, do not contribute to the meridional transport. The meridional transport of PV by the eddies is really insensitive to the details of the turbulence at the mesoscale and submesoscale. This is also the scale at which the meridional heat transport occurs where $\langle v, b \rangle$ (not shown) is positive.

c. Meridional circulation

We now present the three meridional (secondary) circulations: the Eulerian circulation (EC), the eddy-induced circulation (EIC), and the residual circulation (RC). They stem from the zonal and time averaging (denoted by an overbar) of the buoyancy equation,

$$\partial_t \overline{b} = 0 = -\overline{w} - N^{-2}\partial_y \overline{v'b'} + N^{-2}\overline{F}_b, \quad (23)$$

where $\overline{v'b'}$ is the meridional eddy buoyancy flux. Each term of the RHS corresponds to a streamfunction
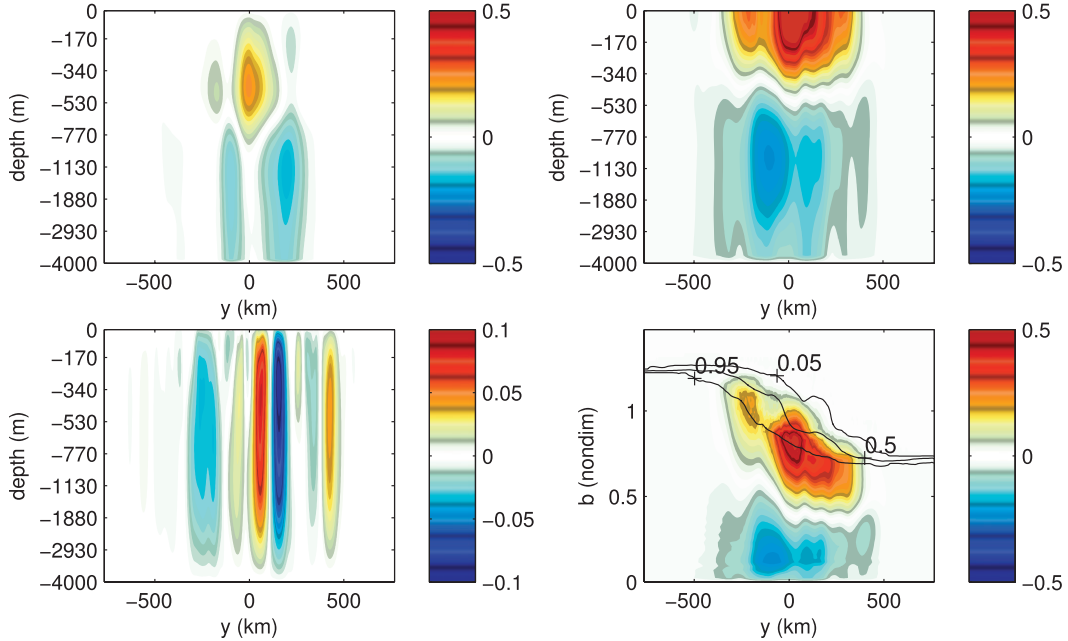
FIG. 13. EIC in z coordinates for (top left) the Phillips and (top right) the Charney regimes, EC for (bottom left) the Charney regime, and (bottom right) EIC for the Charney regime in isopycnal coordinates. Units are in Sverdrups ($1 \text{ Sv} \equiv 10^6 \text{ m}^3 \text{ s}^{-1}$). Buoyancy axis has been nondimensionalized by the mean value at surface. The contours in (bottom right) indicate the isolines of the PDF $P(y, b)$ for a parcel of buoyancy b at position y to never reach the surface. The surface layer corresponds to $P(y, b) < 1$.

$$\overline{\Psi} = \int^y \overline{w} \, dy, \quad \Psi^* = N^{-2}\overline{v'b'}, \quad \Psi_r = -N^{-2}\int^y \overline{F}_b \, dy, \tag{24}$$

where $\overline{\Psi}$ is the EC, Ψ^* is the EIC, and Ψ_r is the RC. By construction, (23) ensures $\overline{\Psi} + \Psi^* + \Psi_r = 0$. The numerical convergence of these quantities is achieved by time averaging over 200 days directly online (Fig. 13). The most striking feature is the weakness of EC compared to EIC for both regimes. The main balance is $\Psi^* + \Psi_r \sim 0$, which is at odds with the SO, where the leading-order balance is $\overline{\Psi} + \Psi^* \sim 0$ (Marshall and Radko 2003). This difference is due to the absence of a wind forcing in the experiments. In the SO, the strong EC arises as a result of the Ekman pumping (Speer et al. 2000; Abernathey et al. 2011). The spatial structure of the EC is also unrealistic: it is composed of several narrow overturning cells (with a meridional scale of the order of L_d), but in the SO it is a unique wide overturning cell, the Deacon cell, several hundreds of kilometers wide (Speer et al. 2000; Marshall and Radko 2003; Abernathey et al. 2011). In the SO, the EC tends to build up the meridional isopycnal slope; the Ekman pumping is the source of APE for the BCI. In contrast, the source of APE in these experiments is replaced by the diabatic in situ forcing term F_b. This explains why the RC dominates over the EC in these experiments. The spatial structure of the RC reflects the location of the

diapycnal terms. They should be vanishing in the interior and mainly located close to the surface. This is not the case. Consequently, in the interior the RC is too diabatic and streamlines do not coincide with isopycnals. Not surprisingly, EIC enters at leading order in the balance. The eddies tend to relax the meridional isopycnal slope. This is an evidence of BCI at play.

The two regimes differ by the magnitude of the circulations, with a factor of ~4, consistent with the results on the energetics. They also strongly differ by their vertical structure. In the Phillips case, Ψ^* has closed streamlines at the surface. The interpretation in terms of EIC is straightforward: eddies tend to flatten the isopycnals; they transport heat from the warm side to the cold side of the channel. In the Charney case, the definition (24) yields Ψ^* with open streamlines at the surface. In this case, Ψ^* cannot be interpreted as the EIC because eddies do not advect heat across the surface. The surface should be a streamline of EIC and there should be a return flow somewhere. It is worth emphasizing that, despite the singularity of PV at the surface, the return flow of the EIC does not occur in an infinitely thin surface layer, but it occurs over a finite depth. The buoyancy and the velocities are absolutely smooth and so is the RC. This issue comes from $\overline{v'b'}$ being maximum at the surface (whereas it is strictly zero in the Phillips case). A solution consists in defining

$\Psi^* = \overline{w'b'/b_y}$, which guarantees a closed streamline at the surface. Marshall and Radko (2003) showed this gives satisfactory results for the SO. However, $w'b'$ is a neglected term in the QG equation for buoyancy making it a less natural candidate for EIC. Another solution consists in diagnosing the secondary circulations in isopycnal coordinates. Held and Schneider (1999) showed that the analog of the RC in isopycnal coordinates is

$$\Psi_{\text{iso}}(y,b) = \overline{\int_0^{Z(x,y,b,t)} v\,dz}, \qquad (25)$$

where $Z(x, y, b, t)$ is the isopycnal depth. By construction, the depth-integrated flow vanishes everywhere so Ψ_{iso} has a closed streamline at the surface. However, the top boundary in isopycnal coordinates is fuzzy because the surface buoyancy varies in space and time. This is best handled by the concept of surface layer (Held and Schneider 1999): for a given y, there is a set of isopycnals that sometimes outcrop. Practically, it is computed by associating with each point (y, b_0) the probability density function $P(y, b_0)$ that $b(x, y, 0, t) > b_0$. The surface layer is then the region where $P(y, b) < 1$, and the interior corresponds to $P(y, b) = 1$; the surface layer is the region where the fluid can reach the surface.

This isopycnal diagnostic can be generalized to the EIC as follows: We replace the equation for b by the equation for $Z(b)$,

$$\partial_t Z = w - J(\psi, Z) + w_F, \qquad (26)$$

where $w_F = -N^{-2}F_b$ is the diapycnal vertical velocity associated with the buoyancy forcing. Using the same procedure as between (23) and (24), we can associate $\overline{\Psi}(y,b), \Psi^*(y,b)$, and $\Psi_r(y,b)$ with each term of the RHS of (26). The EIC in isopycnal coordinates then is

$$\Psi^*(y,b) = \int^y \overline{J(\psi,Z)}\,dy, \qquad (27)$$

where the integrand is taken along the isopycnal b. The EIC is now physically sound, with a return flow taking place within the surface layer (Fig. 13). In the interior, both isopycnal and z coordinates yield the same EIC. As in the Phillips case, the EIC tends to flatten the isopycnals. Incidentally, $\Psi^*(y, b)$ is a robust quantity, independent of the gauge choice, because it does not explicitly depend on the forcing. This offers another interpretation of the gauge issue. The gauge impacts the partition between $\overline{\Psi}$ and Ψ_r, but their sum $(-\Psi^*)$ is fixed. Another gauge choice could have been to minimize F_b instead of minimizing w.

By varying the control parameter of the experiment, the EIC is continuously transformed from the Phillips case to the Charney case; there is no qualitative bifurcation. However, the surface layer occurs as soon as there is an outcropping of isopycnals. In this respect, the Phillips case is very particular.

7. Conclusions

We compared two regimes of QG baroclinic turbulence. They differ by their large-scale APE reservoir: the Charney case has a maximum of APE near the surface, whereas the Phillips case has a maximum in subsurface and no APE at the surface. There is a qualitative difference between the two regimes on the mesoscale and submesoscale near the surface. The Charney case is more energetic and has shallower energy spectra near the surface ($\sim k^{-2}$), and its vorticity is locally large with the extremum value depending on the resolution. This regime has properties close to the recent high-resolution simulations conducted with a PE model (Klein et al. 2008). The Phillips case is more like the traditional QG regime with a low level of submesoscale turbulence. Its properties are almost insensitive to the resolution. These differences can be traced back to the properties of the BCI. There is a finite band of unstable modes in the Phillips case and a semi-infinite band in the Charney case. Thus, there is a well-defined bifurcation between the two regimes, at least in the BCI linear stability analysis. This semi-infinite band of unstable modes is responsible for energizing the submesoscale in the Charney case.

We analyzed the enstrophy and the energy budgets in the (k, z) plane. In both regimes, the enstrophy is input at the largest scales and cascades to small scales, where it is dissipated. The energy budget is richer than previously shown by the literature (Salmon 1980; Larichev and Held 1995). Because there is no wind in the experiment, energy is input at the largest scale by the buoyancy forcing in the APE reservoir. APE cascades forward everywhere. It is entirely converted into KE at some scale, depending on the depth. This APE is then fluxed upward by the pressure field and transformed into KE. The KE cascades backward to the scale of arrest (250 km). A small fraction ($\approx 10\%$) goes through larger scales; another fraction is dissipated at the bottom through Ekman damping; and the main fraction is converted back to APE at depth. Thus, the external forcing sustains an inner energy cycle that is more vigorous than the forcing with an efficiency of 3.3 for the Charney case and 2.5 for the Phillips case. This energy cycle is a new result and completes the Salmon (1980) picture. In these experiments, the scale of arrest is set by β, not by the bottom friction. It is larger—but not much larger—than the deformation scale. Thus, in the Phillips case the inverse cascade of KE occurs on a narrow band, contrasting with the Charney case. We have also confirmed

TABLE A1. Parameters of the experiments.

f	Coriolis parameter	10^{-4} s^{-1}
β	beta parameter	$1.56\ 10^{-11}$ m^{-1} s^{-1}
L	zonal width	768 km
H	depth	4 km
L_d	deformation radius	96 km
L_{jet}	width jet	800 km
γ	memory constant for the forcing	1/50 day^{-1}
L_s	meridional smoothing width for the forcing	600 km
τ	time restoring to the reference jet	50 days
λ	Ekman damping	100 days
U^*	criticality	0.6

recent results showing that there is no cascade in QG for the volume-integrated energy beyond the scale of arrest at large Reynolds number (Molemaker et al. 2010); for finite resolution and in the Charney case, there is a small part that is carried to the submesoscale near the surface where it is dissipated. It implies a tendency toward QG inconsistency by producing a shallow spectrum near the surface. The Charney case is more energetic than the Phillips case.

In the two regimes, the large-scale buoyancy forcing is balanced by a meridional eddy PV flux. This transport is entirely done at the scale of arrest. The eddy diffusivity is quite nonuniform, with a maximum where the pool of negative Q_y. The Charney case has larger diffusivities than the Phillips case. The qualitative bifurcation between the two regimes is not associated with the presence of outcropping but with the vertical location of $Q_y < 0$.

One of the central questions that is still pending is how the flow adjusts its mean state and its level of turbulence to the external forcing. We hope to address this in a subsequent paper.

APPENDIX A

Numerical Details

a. Parameters of the study

Table A1 summarizes the parameters we used. The horizontal dimensions of the channel $L \times 2L$ have been chosen to be a multiple of the deformation radius L_d, $L_d = L_x/8 = L_y/16$.

b. QG model

The variables are discretized on a staggered grid. The streamfunction is localized at the vertices of the cells. The advected PV is face centered. It is interpolated bilinearly at the vertices for the inversion stage. We explicitly distinguish the interior PV at the surface from the surface PV, although they are located at the same place. The lateral boundary condition is taken directly into account in the elliptic operator: the Laplacian returns a single value (the circulation) for all the points along a wall. The inversion is done with a full multigrid cycle. The model is fully parallelized. We developed a special technique to both (i) minimize messages passing on coarse grids during the multigrid inversion and (ii) cope with the fact that, at high resolution, there are more nodes than grid points on the coarser grid. This technique consists in clustering the subdomains together on the same node as the grid is coarsened. This procedure allows the performance to follow the expected theoretical speedup. The time step is smoothly varied in time so that the CFL number is always close to an assigned value (0.3 in our experiments). We report that nonsmooth variations of the time step artificially increase the dissipation.

APPENDIX B

Diagnostics

a. Numerical dissipation

The dissipation of PV D_q is estimated solely from the discretized advection scheme. With $J(\psi, q)$ the discretized Jacobian, we define D_q and the inviscid Jacobian $J^*(\psi, q)$ by

$$D_q = -\frac{1}{2}[J(\psi^{n+1/2}, q^{n+1/2}) + J(-\psi^{n+1/2}, q^{n+1/2})]$$

$$J^*(\psi, q) = \frac{1}{2}[J(\psi^{n+1/2}, q^{n+1/2}) - J(-\psi^{n+1/2}, q^{n+1/2})].$$

(B1)

This ensures that $J(\psi, q) = J^*(\psi, q) - D_q$. We interpret D_q as the time irreversible part of the discretized advection. To our knowledge, this diagnostic is new. With the same goal, Molemaker et al. (2010) used a second-order enstrophy-conserving scheme to compute J^*. We think our approach is better, because it avoids introducing extra errors due to this extra advection scheme.

b. Ageostrophic velocity

The vertical velocity w_a is computed by the residual of the two close terms,

$$N^2(z)w_a = \partial_z \mathbf{L}^{-1} J^*(\psi, \partial_z \psi) - J^*(\psi, \partial_z \psi) \quad \text{(B2)}$$

(u_a and v_a are computed in the same manner, replacing ∂_z by ∂_x and ∂_y), where J^* is a nondissipative Jacobian. The computed velocity is insensitive to the choice of this Jacobian. We can either use the previous inviscid Jacobian or a second-order enstrophy-conserving one. We chose this latter because it is computationally cheaper. Again, this diagnostic is new to our knowledge. It is much easier to implement than the omega equation, because the elliptic operator to invert is the PV operator. The obtained field is also smoother than by taking the residual of $\partial_t b + J(\psi, b)$. This diagnostic stems from

$$\partial_t \psi = \mathbf{L}^{-1} \partial_t q = \mathbf{L}^{-1}[F_q + D_q - J^*(\psi, q)], \quad \text{(B3)}$$

and then differentiating in z and adding explicitly the advection of buoyancy yields (B2).

c. Spectra and cospectra

The cospectrum $\langle a, b \rangle$ of the two variables (a, b) is computed by (i) detrending and applying a Hanning window in the y direction on each variable, (ii) 2D Fourier transforming them, (iii) azimuthal summing the real part of their product over an annulus of radius k and width 1, and (iv) correcting for the irregular number of points from one discretized annulus to the other. The cospectrum is then averaged over 20 snapshots, sampling a time interval of 200 days. This time averaging is designed to smooth the cospectra and also to cancel the time derivative term in the budget (either of enstrophy, KE, or APE). Note that we never compute directly the cospectrum of the advective terms (corresponding to the nonlinear transfer across horizontal scales) because it is highly noisy. Spectra (enstrophy, KE, and APE) are computed in the same manner as they are basically cospectra of the variable with itself.

d. Forcing and dissipation

Conversely, it is possible to switch back by inverting the elliptic equation then taking the 3D gradient. Using these relationships, we relate the forcing and dissipation for PV to those for momentum and buoyancy by introducing the potentials Φ and Ω,

$$\Phi = \mathbf{L}^{-1} F_Q, \quad \Omega = \mathbf{L}^{-3} D_Q \quad \text{and} \quad \text{(B4)}$$

$$F_{u,v,b} = \partial_{x,y,z} \Phi, \quad D_{u,v,b} = \partial_{x,y,z} \Omega, \quad \text{(B5)}$$

where $\mathbf{L}$ is the elliptic operator for the PV inversion.

REFERENCES

Abernathey, R., J. Marshall, M. Mazloff, and E. Shuckburgh, 2010: Enhancement of mesoscale eddy stirring at steering levels in the Southern Ocean. *J. Phys. Oceanogr.,* **40,** 170–184.

——, ——, and D. Ferreira, 2011: The dependence of Southern Ocean meridional overturning on wind stress. *J. Phys. Oceanogr.,* **41,** 2261–2278.

Blumen, W., 1978: Uniform potential vorticity flow: Part I. Theory of wave interactions and two-dimensional turbulence. *J. Atmos. Sci.,* **35,** 774–783.

Bretherton, F. P., 1966: Critical layer instability in baroclinic flows. *Quart. J. Roy. Meteor. Soc.,* **92,** 325–334.

Capet, X., P. Klein, B. L. Hua, G. Lapeyre, and J. C. McWilliams, 2008a: Surface kinetic energy transfer in surface quasi-geostrophic flows. *J. Fluid Mech.,* **604,** 165–174.

——, J. C. McWilliams, M. J. Molemaker, and A. F. Shchepetkin, 2008b: Mesoscale to submesoscale transition in the California Current system. Part III: Energy balance and flux. *J. Phys. Oceanogr.,* **38,** 2256–2269.

Charney, J. G., 1947: The dynamic of long waves in a baroclinic westerly current. *J. Meteor.,* **4,** 135–162.

Gill, A. E., J. S. A. Green, and A. J. Simmons, 1974: Energy partition in the large-scale ocean circulation and the production of mid-ocean eddies. *Deep-Sea Res. I,* **21,** 499–528.

Green, J. S. A., 1970: Transfer properties of the large-scale eddies and the general circulation of the atmosphere. *Quart. J. Roy. Meteor. Soc.,* **96,** 157–185.

Held, I. M., and V. D. Larichev, 1996: A scaling theory for horizontally homogeneous, baroclinically unstable flow on a beta plane. *J. Atmos. Sci.,* **53,** 946–952.

——, and T. Schneider, 1999: The surface branch of the zonally averaged mass transport circulation in the troposphere. *J. Atmos. Sci.,* **56,** 1688–1697.

——, R. T. Pierrehumbert, S. T. Garner, and K. L. Swanson, 1995: Surface quasi-geostrophic dynamics. *J. Fluid Mech.,* **282,** 1–20.

Hogg, A. M. C., and J. R. Blundell, 2006: Interdecadal variability of the Southern Ocean. *J. Phys. Oceanogr.,* **36,** 1626–1645.

Killworth, P., 1997: On the parameterization of eddy transfer Part I. Theory. *J. Mar. Res.,* **55,** 1171–1197.

Klein, P., B. L. Hua, G. Lapeyre, X. Capet, S. Le Gentil, and H. Sasaki, 2008: Upper ocean turbulence from high-resolution 3D simulations. *J. Phys. Oceanogr.,* **38,** 1748–1763.

Larichev, V. D., and I. M. Held, 1995: Eddy amplitudes and fluxes in a homogeneous model of fully developed baroclinic instability. *J. Phys. Oceanogr.,* **25,** 2285–2297.

Marshall, J., and T. Radko, 2003: Residual-mean solutions for the Antarctic Circumpolar Current and its associated overturning circulation. *J. Phys. Oceanogr.,* **33,** 2341–2354.

——, D. Olbers, H. Ross, and D. Wolf-Gladrow, 1993: Potential vorticity constraints on the dynamics and hydrography of the Southern Ocean. *J. Phys. Oceanogr.,* **23,** 475–487.

McWilliams, J. C., and J. H. S. Chow, 1981: Equilibrium geostrophic turbulence I: A reference solution in a β-plane channel. *J. Phys. Oceanogr.,* **11,** 921–949.

——, F. Colas, and M. J. Molemaker, 2009: Cold filamentary intensification and oceanic surface convergence lines. *Geophys. Res. Lett.,* **36,** L18602, doi:10.1029/2009GL039402.

Miles, J. W., 1964: Baroclinic instability of the zonal wind. *Rev. Geophys.,* **2,** 155–176.

Molemaker, M. J., J. C. McWilliams, and X. Capet, 2010: Balanced and unbalanced routes to dissipation in an equilibrated Eady flow. *J. Fluid Mech.,* **654,** 35–63.

Phillips, N., 1954: Energy transformations and meridional circulations associated with simple baroclinic waves in a two-level, quasi-geostrophic model. *Tellus,* **6,** 273–286.

Salmon, R. S., 1980: Baroclinic instability and geostrophic turbulence. *Geophys. Astrophys. Fluid Dyn.,* **15,** 167–211.

Shchepetkin, A. F., and J. C. McWilliams, 2005: The Regional Oceanic Modeling System: A split-explicit, free-surface, topography-following-coordinate ocean model. *Ocean Modell.,* **9,** 347–404.

Smith, K. S., 2007: The geography of linear baroclinic instability in Earth's oceans. *J. Mar. Res.,* **65,** 655–683.

——, and G. K. Vallis, 2002: The scales and equilibration of mid-ocean eddies: Forced–dissipative flow. *J. Phys. Oceanogr.,* **32,** 1699–1720.

——, and J. Marshall, 2009: Evidence for enhanced eddy mixing at middepth in the Southern Ocean. *J. Phys. Oceanogr.,* **39,** 50–69.

Speer, K., S. R. Rintoul, and B. Sloyan, 2000: The diabatic Deacon cell. *J. Phys. Oceanogr.,* **30,** 3212–3222.

Stammer, D., 1997: Global characteristics of ocean variability estimated from regional TOPEX/Poseidon altimeter measurements. *J. Phys. Oceanogr.,* **27,** 1743–1769.

Thompson, A. F., and W. R. Young, 2006: Scaling baroclinic eddy fluxes: Vortices and energy balance. *J. Phys. Oceanogr.,* **36,** 720–738.

Tréguier, A.-M., and J. C. McWilliams, 1990: Topographic influences on wind-driven, stratified flow in a β-plane channel: An idealized model for the Antarctic Circumpolar Current. *J. Phys. Oceanogr.,* **20,** 321–343.

Tulloch, R., and K. S. Smith, 2009: Quasigeostrophic turbulence with explicit surface dynamics: Application to the atmospheric energy spectrum. *J. Atmos. Sci.,* **66,** 450–467.

——, J. Marshall, and C. Hill, 2011: Scales, growth rates and spectral fluxes of baroclinic instability in the ocean. *J. Phys. Oceanogr.,* **41,** 1057–1076.

Zurita-Gotor, P., and G. K. Vallis, 2009: Equilibration of baroclinic turbulence in primitive equations and quasigeostrophic models. *J. Atmos. Sci.,* **66,** 837–863.